Pairing and chiral spin density wave instabilities on the honeycomb lattice: A comparative quantum Monte Carlo study

Tao Ying[1,2] and Stefan Wessel[1]

[1]*Institut für Theoretische Festkörperphysik, JARA-FIT and JARA-HPC, RWTH Aachen University, 52056 Aachen, Germany*
[2]*Department of Physics, Harbin Institute of Technology, 150001 Harbin, China*

Using finite-temperature determinantal quantum Monte Carlo calculations, we reexamine the pairing susceptibilities in the Hubbard model on the honeycomb lattice, focusing on doping levels onto and away from the Van Hove singularity (VHS) filling. For this purpose, electronic densities of 0.75 (at the hole-doping VHS) and 0.4 (well below the VHS) are considered in detail, where due to a severe sign problem at strong coupling strengths, we focus on the weak-interaction region of the Hubbard model Hamiltonian. By analyzing the temperature dependence of pairing susceptibilities in various symmetry channels, we find the singlet $d + id$ wave to be the dominant pairing channel both at and away from the VHS filling. We furthermore investigate the electronic susceptibility to a specific chiral spin density wave (SDW) order, which we find to be similarly relevant at the VHS, while it extenuates upon doping away from the VHS filling.

I. INTRODUCTION

In recent years, graphene [1–3] has attracted a lot of attention due to its unusual electronic properties. At charge neutrality, corresponding to a half-filled lattice in the Hubbard model description of graphene's π-electron system, a vanishing density of states at the Fermi level (the Dirac points) renders a semimetallic state stable against instabilities from electron-electron interactions, even in the intermediate-coupling regime [4–7]. In contrast, upon doping well away from the Dirac points through chemical doping [8] or electrical gating [9], correlation effects are expected to no longer be limited to the strong-interaction regime. Indeed, various possible phases, such as superconducting instabilities, magnetism, and charge/spin density waves, have been considered to emerge in doped graphene: Several theoretical studies focused on superconducting states of correlated electrons on the honeycomb lattice of graphene, mainly within a local Hubbard model description [10]. Based on mean-field theory, Black-Schaffer and Doniach [11] suggest that graphene may become a $(d + id)$-wave superconductor over a wide range of doping, while Uchoa and Castro Neto [12] suggest extended s-wave and $(p + ip)$-wave pairing states. Functional renormalization group (FRG) theory calculations proposed f-wave and $(d + id)$-wave instabilities [13], and variational Monte Carlo [14,15] and auxiliary-field quantum Monte Carlo studies [16] both support $(d + id)$-wave pairing, while a variational cluster approximation and a cellular dynamical mean-field theory study [17] suggest a $p + ip$ pairing symmetry. In general, this problem is far from having a conclusion. An even more peculiar condition is obtained upon doping the electronic system onto the Van Hove singularity (VHS), where the noninteracting extended Fermi surface exhibits perfect nesting. As a consequence, the pairing mechanism may be different from the one at more generic doping levels [18,19], and furthermore, the electronic system might even host other types of orders, such as a Pomeranchuk

instability [20] or a chiral spin density wave (SDW) order [21]. Different scenarios have indeed been proposed: A renormalization group study finds $d + id$ pairing at the VHS filling in the weak-coupling limit [22]. Using an FRG approach, Wang *et al.* obtained a chiral SDW in the intermediate-interaction region at the VHS filling, while $d + id$ pairing was obtained away from the VHS [23]. Another FRG study reports possible $d + id$ or SDW instabilities in the intermediate-interaction region at the VHS and $(d + id)$- or f-wave pairing away from the VHS [24]. More recently, a dynamic cluster approximation study suggested that the $(d + id)$-wave pairing state dominates in the weak-coupling regime, while for stronger interactions, a $(p + ip)$-wave state strongly competes with the $(d + id)$-wave state [25]. However, in this study, SDW instabilities have not been considered. This state of affairs motivated us to examine this problem using finite-temperature determinantal quantum Monte Carlo (FT-DQMC), an essentially unbiased numerical algorithm. The rest of this paper is organized as follows: In Sec. II, we introduce the model that we consider and outline the FT-DQMC approach. Then we analyze in Sec. III various pairing channels of superconducting instabilities, while in Sec. IV, we consider the chiral SDW instability and contrast its behavior with other magnetic ordering channels. Finally, we summarize our results in Sec. V.

II. MODEL AND METHOD

In this paper, we examine the effective pairing susceptibility for various different pairing channels and identify the dominant pairing channel for doping levels onto and away from the VHS. Moreover, we also consider the chiral SDW instability that was proposed by Li [21] and examine to what extent this chiral SDW instability affects the behavior at the VHS filling and upon doping away from the VHS point. For this analysis, we consider the Hubbard model on the honeycomb lattice to
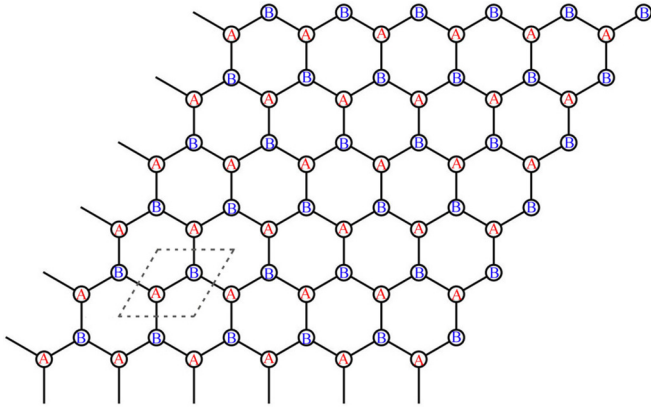
FIG. 1. Rhombic honeycomb lattice geometry for $L = 6$, with $N_s = 72$ sites. Dashed lines enclose the two-site unit cells, and the bipartite sublattice structure is indicated by site-centered letters A and B.

describe the doped graphene system. This model is given in terms of the Hamiltonian

$$H = -t \sum_{\langle \mathbf{i}, \mathbf{j} \rangle \sigma} (c_{\mathbf{i}\sigma}^\dagger c_{\mathbf{j}\sigma} + c_{\mathbf{j}\sigma}^\dagger c_{\mathbf{i}\sigma}) + U \sum_{\mathbf{i}} n_{\mathbf{i}\uparrow} n_{\mathbf{i}\downarrow}$$
$$- \mu \sum_{\mathbf{i}} (n_{\mathbf{i}\uparrow} + n_{\mathbf{i}\downarrow}), \qquad (1)$$

where t is the fermion hopping amplitude between nearest-neighbor sites on the honeycomb lattice (here, $\mathbf{i}$ and $\mathbf{j}$ denote lattice vectors), U denotes an on-site repulsion, and μ is the chemical potential that allows us to tune the electron density, denoted ρ in the following. We work in units of $t = 1$ in the following.

The numerical algorithm used in this paper is the FT-DQMC method [26,27]. We consider finite rhombic clusters of the bipartite honeycomb lattice with periodic boundary conditions and with $N_s = L \times L \times 2$ lattice sites, mainly for $L = 6$ and $L = 12$ in order to ensure that both the K (Dirac) and M points of the hexagonal Brillouin zone are included in the discrete lattice momentum space. Close to the VHS filling, we also consider other even linear system sizes such as $L = 10$ and $L = 14$ (for even L, the M points are included in the discrete lattice momentum space). The finite lattice geometry for $L = 6$ in real space is shown in Fig. 1. The simulations were performed at finite temperatures, and we then analyzed the observed tendencies upon lowering the temperature. In the following, we are mainly interested in the doping level of the VHS, where the electron density is $\rho = 0.75$ or $\rho = 1.25$. Due to particle-hole symmetry, we considered the case of $\rho = 0.75$ explicitly.

However, upon doping beyond half filling, the FT-DQMC method suffers from a severe sign problem, which worsens upon lowering the temperature and increasing the interaction strength [28]. To quantify the sign problem of the FT-DQMC in the relevant parameter regime, we show in Fig. 2 the dependence of the average sign, denoted $\langle \text{sign} \rangle$, on the interaction strength U, the density ρ, and the temperature T for different lattice sizes. As Monte Carlo errors decrease with the square root of the number of independent samples, it is necessary to run a simulation code 100 times longer to compensate,
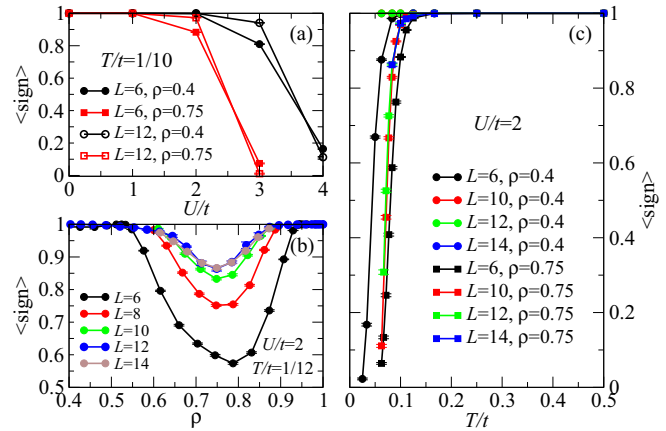

FIG. 2. The average FT-DQMC sign, $\langle \text{sign} \rangle$, for different lattice sizes as a function of (a) interaction strength U, (b) density ρ, and (c) temperature T.

for example, for an average sign of 0.1. Figure 2(a) shows that at the VHS filling of $\rho = 0.75$, the average sign rapidly drops to values below 0.1 beyond $U = 2t$ at the considered temperature of $T/t = 1/10$. Furthermore, a dip in $\langle \text{sign} \rangle$ at the VHS filling of $\rho = 0.75$ is seen in the density dependence of $\langle \text{sign} \rangle$ in Fig. 2(b) for $U/t = 2$. For the considered temperature of $T/t = 1/12$, this dip is more pronounced for the smaller system sizes, while the average sign appears to converge upon increasing L at this fixed temperature to a still conveniently large value. However, as seen from Fig. 2(c), the average sign shows a rapid drop with decreasing temperature also for $U/t = 2$, which restricts us from accessing true ground-state properties on large systems near the VHS filling.

Hence, depending on the doping level and in particular near the VHS filling, we restricted our investigation to the weak- to intermediate-interaction regime in order to still access low temperatures that allow us to identify the onset of divergences in the pairing or magnetic susceptibilities. Furthermore, in order to compare the results for the VHS filling with those at more generic fillings, we also performed further simulations at $\rho = 0.4$, i.e., a doping level far below the VHS filling, where the sign problem is less severe, and we can extend a bit farther towards the stronger-interaction regime.

III. PAIRING CORRELATIONS

In order to probe for superconducting instabilities, we examine the system's susceptibility towards various previously proposed pairing channels for this model. In particular, we consider the nearest-neighbor (NN) extended s-wave, $(d + id)$-wave, and $(p + ip)$-wave pairing correlations and consider also next-nearest-neighbor (NNN) $(d + id)$-wave, $(p + ip)$-wave, and f-wave pairings. In real space, these different pairing channels are given in terms of appropriate form factors,

$$f_{\text{NN},es}(\boldsymbol{\delta}_l) = 1, \quad f_{\text{NN},d+id}(\boldsymbol{\delta}_l) = e^{i(l-1)\frac{2\pi}{3}},$$

$$f_{\text{NN},p+ip}(\boldsymbol{\delta}_l) = e^{i(l-1)\frac{2\pi}{3} + \epsilon_s i\pi},$$

$$f_{\text{NNN},d+id}(\boldsymbol{\delta}_l') = e^{i(l-1)\frac{2\pi}{3}}, \quad f_{\text{NNN},p+ip}(\boldsymbol{\delta}_l') = e^{i(l-1)\frac{\pi}{3}},$$

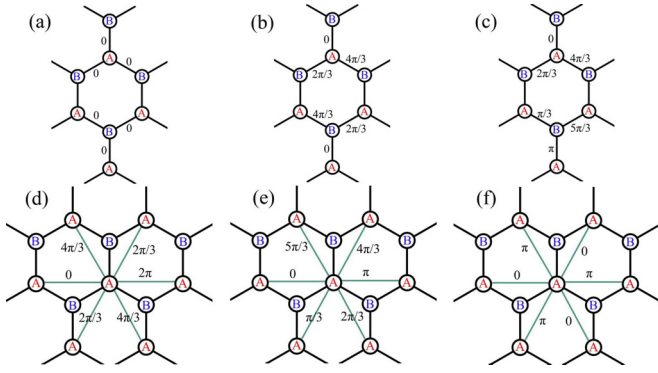$$f_{\text{NNN},f}(\boldsymbol{\delta}_l') = e^{i\frac{1+(-1)^l}{2}\pi}, \qquad (2)$$

FIG. 3. Phases of the considered pairing channels along the corresponding directions on the honeycomb lattice: (a) NN extended s wave, (b) NN $d + id$ wave, (c) NN $p + ip$ wave, (d) NNN $d + id$ wave, (e) NNN $p + ip$ wave, and (f) NNN f-wave.

where the vectors $\boldsymbol{\delta}_l, l = 1, 2, 3$ ($\boldsymbol{\delta}'_l, l = 1, 2, \ldots, 6$) denote the different NN (NNN) lattice directions from a given lattice site and $\epsilon_s = 0$ (1) for sites on the A (B) sublattice. Figure 3 shows these various form factors explicitly. In the spin sector, the s and d waves are singlet states, while p and f waves are triplet states. The corresponding local pairing operators are thus given as

$$\Delta_{\alpha \mathbf{i}} = \frac{1}{\sqrt{N_\alpha}} \sum_l f_\alpha(\boldsymbol{\delta}_l^{(\prime)})\big(c_{\mathbf{i}\uparrow} c_{\mathbf{i}+\boldsymbol{\delta}_l^{(\prime)}\downarrow} \pm c_{\mathbf{i}\downarrow} c_{\mathbf{i}+\boldsymbol{\delta}_l^{(\prime)}\uparrow}\big), \quad (3)$$

where the plus (minus) sign is for triplet (singlet) pairing and N_α are the corresponding normalization factors, with $N_\alpha = 3$ ($N_\alpha = 6$) for the NN (NNN) channels.

Within the QMC simulations, we can directly access the temperature dependence of the pairing susceptibilities for the various channels,

$$P_\alpha = \frac{1}{N_s} \sum_{\mathbf{i}, \mathbf{j}} \int_0^\beta d\tau \, \langle \Delta_{\alpha \mathbf{i}}^\dagger(\tau) \Delta_{\alpha \mathbf{j}}(0) \rangle, \quad (4)$$

where $\Delta_{\alpha \mathbf{i}}^\dagger(\tau) = e^{\tau H} \Delta_{\alpha \mathbf{i}}^\dagger(0) e^{-\tau H}$. These pairing susceptibilities are, however, strongly affected by the enhanced response of the free system at $U = 0$. This behavior is illustrated in Fig. 4, which shows the different susceptibilities P_α as functions of T on the $L = 6$ lattice for both $\rho = 0.4$ and $\rho = 0.75$ in the noninteracting limit $U = 0$. While there are no superconducting ground states in the noninteracting case, the apparent divergence of P_α upon lowering T provides a background to the susceptibility measurements in the interacting case, in particular in the low-coupling regime that we can access in the FT-DQMC simulations. We thus need to examine the various pairing channels based on the effective pairing interaction vertex [29]. In order to extract the corresponding effective pairing susceptibilities, we compute in FT-DQMC also the bare pairing contributions $\tilde{P}_\alpha$, for which two-particle terms $\langle c_{\mathbf{i}\downarrow}^\dagger(\tau) c_{\mathbf{j}\downarrow}(0) c_{\mathbf{k}\uparrow}^\dagger(\tau) c_{\mathbf{l}\uparrow}(0) \rangle$ that appear in evaluating P_α in Eq. (4) are replaced by the decoupled contributions $\langle c_{\mathbf{i}\downarrow}^\dagger(\tau) c_{\mathbf{j}\downarrow}(0) \rangle \langle c_{\mathbf{k}\uparrow}^\dagger(\tau) c_{\mathbf{l}\uparrow}(0) \rangle$. The effective pairing susceptibilities are then given as $P_\alpha^{\text{eff}} = P_\alpha - \tilde{P}_\alpha$, where a positive (negative) value of P_α^{eff} signals an enhanced (suppressed)
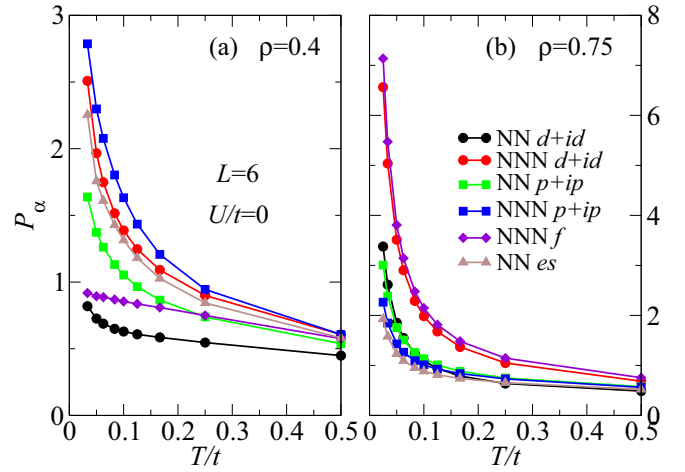

FIG. 4. Temperature dependence of the various pairing susceptibilities P_α for the noninteracting system ($U = 0$), as obtained on an $L = 6$ system for (a) $\rho = 0.4$ and (b) $\rho = 0.75$.

tendency towards pairing in the corresponding channel. By definition, for the noninteracting case, P_α^{eff} vanishes.

We now examine the interacting system and begin with the case of an electron density $\rho = 0.4$, i.e., well below the VHS filling. First, we consider the results obtained for the $L = 6$ lattice with 72 sites. At this density the sign problem is sufficiently moderate, and we can obtain P_α^{eff} up to $U/t = 4$, as shown in Figs. 5(a) to 5(d) for $U/t = 1$ to $U/t = 4$, respectively. These results for the $L = 6$ lattice show that, consistently, both the NN and NNN $(d + id)$-wave pairing susceptibilities are enhanced upon lowering T for all the considered interaction strengths. (We also measured the extended s-wave channel susceptibility, but it is rather strongly suppressed in all the interacting cases that we considered, and we thus do not include it in Fig. 5 or any of the figures below.)

To assess the stability of this result with respect to finite-size effects, we also performed simulations on the $L = 12$ system with 288 sites, i.e., four times larger than the $L = 6$ lattice. Since in Fig. 5 we find the prevailing pairing channel does not
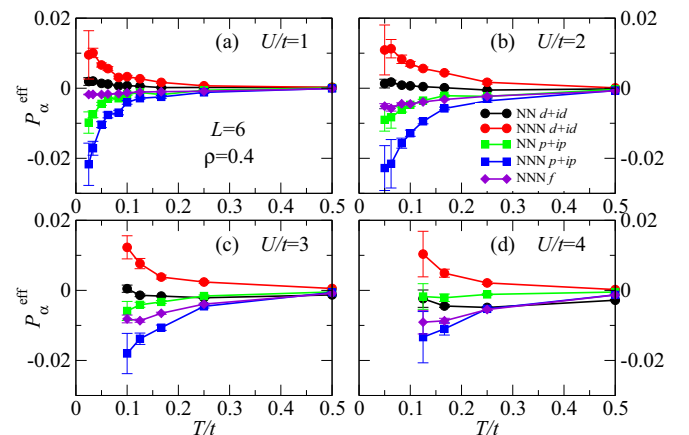

FIG. 5. Temperature dependence of the effective pairing susceptibilities P_α^{eff} at density $\rho = 0.4$ on the $L = 6$ lattice for (a) $U/t = 1$, (b) $U/t = 2$, (c) $U/t = 3$, and (d) $U/t = 4$.
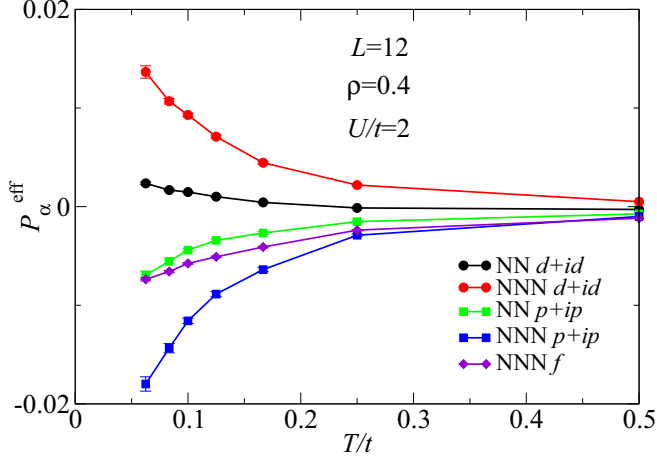
FIG. 6. Temperature dependence of the effective pairing suscep-
tibilities P_α^{eff} at density $\rho = 0.4$ on the $L = 12$ lattice for $U/t = 2$.

FIG. 8. Temperature dependence of the effective pairing suscepti-
bilities at the VHS filling ($\rho = 0.75$) on the $L = 10, 12$, and 14 lattices
for (a) $U/t = 1$ and (b) $U/t = 2$.

depend on the interaction strengths at $\rho = 0.4$, we concentrate
in Fig. 6 on the case of $U/t = 2$ for the $L = 12$ lattice. For
$\rho = 0.4$, the results on the $L = 12$ lattice are in accord with
the findings on the $L = 6$ lattice, and we conclude that $(d + id)$-wave pairing forms the dominant pairing channel in this
doping regime. This is in good agreement with various previous
findings, as mentioned in the Introduction.

We next perform a similar investigation for the VHS filling,
$\rho = 0.75$. Due to the sign problem, we are in this case limited
to weaker interactions and consider explicitly here the cases
of $U/t = 1$ and $U/t = 2$. In contrast to the case of $\rho = 0.4$,
we observe strong finite-size effects at the VHS filling, even
with respect to the leading low-temperature effective pairing
susceptibility: As shown in Fig. 7(a), for a weak coupling of
$U/t = 1$ on the $L = 6$ lattice, upon lowering the tempera-
ture, the effective pairing susceptibility in the NNN f-wave
channel gets strongly enhanced, while all other channels get
suppressed, which suggests f-wave pairing dominates at the
VHS in the weak-coupling region. If the interaction strength is
increased to $U/t = 2$ in Fig. 7(b), the dominant pairing on the
$L = 6$ system still appears in the f-wave channel; however,

the error bars are larger due to a more severe sign problem.
Considering the larger system sizes $L = 10, 12$, and 14 at the
VHS filling, shown in Fig. 8, we instead find, consistently
among these larger system sizes, that the dominant pairing
channel switches from the f wave observed on the $L = 6$
system to the NN and NNN $(d + id)$-wave pairings when the
lattice size is increased. The reason for this behavior may be the
fact that for these larger lattice sizes, we resolve a narrower grid
of momenta within the Brillouin zone, thus better resolving the
effective interactions near the momenta corresponding to the
VHS in the density of states (DOS), which is most important
at the VHS filling.

Another reason for this size dependence may be that due
to the enhanced DOS at the VHS filling, other electronic
instabilities compete with superconductivity. Indeed, based on
a recent mean-field theory [21] and FRG calculations [23], a
particular interesting chiral SDW state was argued to form the
leading magnetic instability of the Hubbard model at the VHS
filling. In the following section, we examine this scenario based
on FT-DQMC simulations.

IV. MAGNETIC CORRELATIONS

The chiral SDW state considered in Refs. [21,23] is charac-
terized by the three independent nesting vectors $\mathbf{Q}_i$, $i = 1, 2, 3$,
of the free system's Fermi surface at the VHS filling, which
(folded back to the first Brillouin zone) correspond to the three
independent M points at the centers of the Brillouin zone edges.
In terms of the reciprocal lattice vectors $\mathbf{b}_1$ and $\mathbf{b}_2$, these are
$\mathbf{Q}_1 = \frac{1}{2}\mathbf{b}_1$, $\mathbf{Q}_2 = \frac{1}{2}\mathbf{b}_2$, and $\mathbf{Q}_3 = \frac{1}{2}(\mathbf{b}_1 + \mathbf{b}_2)$. For lattice sites
on the A and B sublattices within a unit cell centered at position
$\mathbf{R}$, the mean-field expectation values of the local spin operator
in the chiral SDW state are proportional (up to a global rotation
in spin space) to the local direction vectors

$$\langle \mathbf{S}_{\mathbf{R},A} \rangle_{\mathrm{cSDW}} = \frac{1}{\sqrt{3}}(\hat{\mathbf{z}}e^{i\mathbf{Q}_3 \cdot \mathbf{R}} + \hat{\mathbf{x}}e^{i\mathbf{Q}_1 \cdot \mathbf{R}} + \hat{\mathbf{y}}e^{i\mathbf{Q}_2 \cdot \mathbf{R}}),$$

$$\langle \mathbf{S}_{\mathbf{R},B} \rangle_{\mathrm{cSDW}} = \frac{1}{\sqrt{3}}(\hat{\mathbf{z}}e^{i\mathbf{Q}_3 \cdot \mathbf{R}} - \hat{\mathbf{x}}e^{i\mathbf{Q}_1 \cdot \mathbf{R}} - \hat{\mathbf{y}}e^{i\mathbf{Q}_2 \cdot \mathbf{R}}), \quad (5)$$

where $\hat{\mathbf{x}}$, $\hat{\mathbf{y}}$, and $\hat{\mathbf{z}}$ are the three mutually orthogonal unit
vectors in spin space [21]. This state exhibits four different
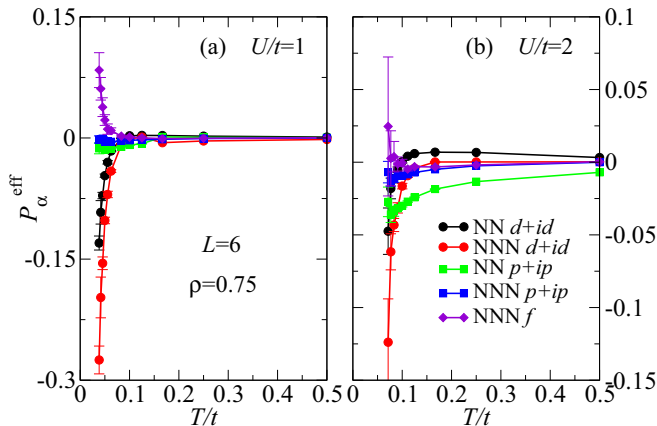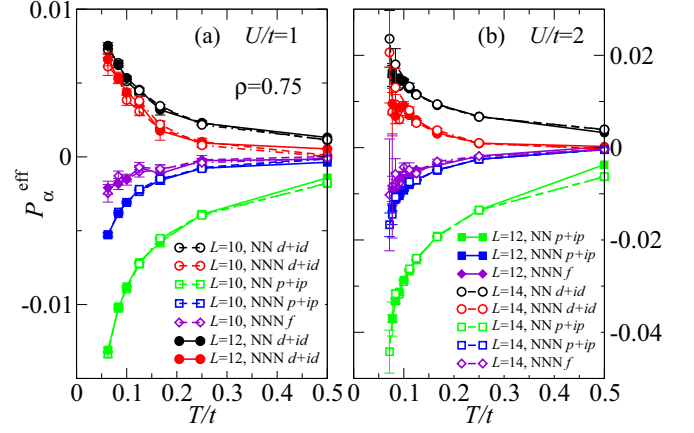

FIG. 7. Temperature dependence of the effective pairing sus-
ceptibilities at the VHS filling ($\rho = 0.75$) on the $L = 6$ lattice for
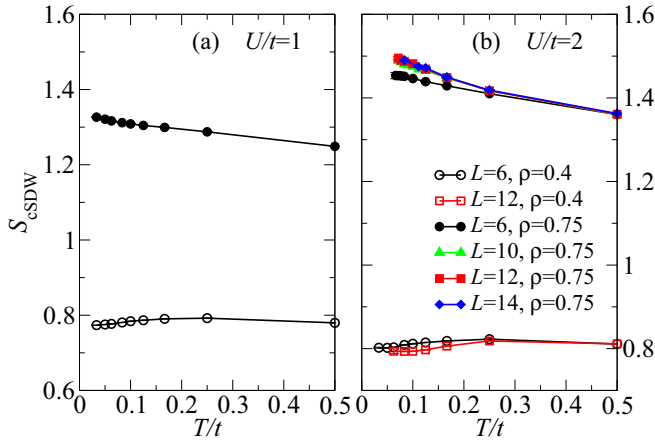(a) $U/t = 1$ and (b) $U/t = 2$.

FIG. 9. Temperature dependence of the structure factor S_{cSDW} at $\rho = 0.75$ and $\rho = 0.4$ for (a) $U/t = 1$ on the $L = 6$ lattice and (b) $U/t = 2$ for lattice sizes $L = 6, 10, 12, 14$.

spin directions, $\hat{x} + \hat{y} + \hat{z}$, $-\hat{x} - \hat{y} + \hat{z}$, $\hat{x} - \hat{y} - \hat{z}$, and $-\hat{x} + \hat{y} - \hat{z}$; the magnetic unit cell thus contains eight lattice sites, and we require L to be even in order to accommodate this spin structure within the finite rhombic clusters. In order to probe for this chiral SDW within the FT-DQMC simulations, we monitor a corresponding structure factor,

$$S_{\text{cSDW}} = \frac{1}{N_s} \left\langle \left(\sum_{\mathbf{R}} M_{\mathbf{R}} \right)^{\dagger} \left(\sum_{\mathbf{R}} M_{\mathbf{R}} \right) \right\rangle, \quad (6)$$

in terms of the projections $M_{\mathbf{R}} = M_{\mathbf{R},\mathbf{A}} + M_{\mathbf{R},\mathbf{B}}$, with $M_{\mathbf{R},\mathbf{A(B)}} = \mathbf{S}_{\mathbf{R},A(B)} \cdot \langle \mathbf{S}_{\mathbf{R},A(B)} \rangle_{\text{cSDW}}$ of the local spin operators on the chiral SDW texture. Here, $\mathbf{S}_{\mathbf{R},A(B)}$ denotes the local spin operator on the A (B) sublattice site within the unit cell at position $\mathbf{R}$; for a lattice site at position $\mathbf{i}$ this is given as $\mathbf{S_i} = \frac{1}{2} \sum_{\alpha,\beta} c_{\mathbf{i},\alpha}^{\dagger} \boldsymbol{\sigma}_{\alpha,\beta} c_{\mathbf{i},\beta}$ in terms of fermionic operators and the vector $\boldsymbol{\sigma}$ of the Pauli matrices. In the following, we also consider for comparison the corresponding antiferromagnetic structure factor S_{AF} for the antiferromagnetic Néel state, which is defined similarly to S_{cSDW}, but with (up to a global spin rotation) $\langle \mathbf{S}_{\mathbf{R},A} \rangle_{\text{AF}} = \hat{z}$ and $\langle \mathbf{S}_{\mathbf{R},B} \rangle_{\text{AF}} = -\hat{z}$. The antiferromagnetic Néel state is well known to emerge in the half-filled system for sufficiently strong interactions. However, here, we first focus on the behavior of the chiral SDW structure factor S_{cSDW}, considering the two specific electronic densities $\rho = 0.75$ and $\rho = 0.4$ like above.

In Fig. 9, we show the FT-DQMC results for S_{cSDW} as functions of T for the two densities, $\rho = 0.75$ and $\rho = 0.4$, at both $U/t = 1$ and $U/t = 2$ on the $L = 6$ lattice. For $U/t = 2$ we also performed simulations on the $L = 12$ lattice (as well as on the $L = 10$ and 14 systems for $\rho = 0.75$) in order to examine the finite-size effect in S_{cSDW}. We find that upon lowering the temperature, S_{cSDW} increases at $\rho = 0.75$, whereas it does not significantly increase and is even weakly suppressed at $\rho = 0.4$. We furthermore observe a mild increase in S_{cSDW} with system size L at the VHS filling $\rho = 0.75$. Since the corresponding magnetic instabilities can occur only at $T/t = 0$ [due to the SU(2) symmetry of the Hamiltonian H], these results suggest that the chiral SDW order, while possibly relevant at $\rho = 0.75$, is not favored at $\rho = 0.4$. A
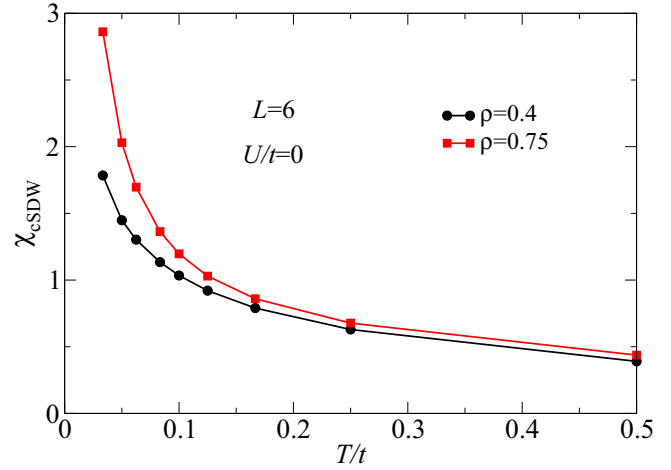

FIG. 10. Temperature dependence of χ_{cSDW} for $\rho = 0.4$ and $\rho = 0.75$ at $U/t = 0$ on the $L = 6$ lattice.

similar picture also emerges from analyzing the corresponding chiral SDW susceptibility

$$\chi_{\text{cSDW}} = \frac{1}{N_s} \int_0^{\beta} d\tau \left\langle \left(\sum_{\mathbf{R}} M_{\mathbf{R}}(\tau) \right)^{\dagger} \left(\sum_{\mathbf{R}} M_{\mathbf{R}}(0) \right) \right\rangle, \quad (7)$$

where $M_{\mathbf{R}}^{\dagger}(\tau) = e^{\tau H} M_{\mathbf{R}}^{\dagger}(0) e^{-\tau H}$. Here, we need to again account for the enhanced response of the free system at $U = 0$. This is shown in Fig. 10: For both densities, χ_{cSDW} at $U = 0$ exhibits an apparent divergence upon lowering the temperature. Like in the case of the pairing susceptibilities, we thus examine the corresponding effective chiral SDW susceptibility, which is obtained as $\chi_{\text{cSDW}}^{\text{eff}} = \chi_{\text{cSDW}} - \tilde{\chi}_{\text{cSDW}}$, where $\tilde{\chi}_{\text{cSDW}}$ denotes the bare chiral SDW susceptibility. This procedure is similar to the antiferromagnetic case considered in Ref. [29].

As shown in Fig. 11 for $U/t = 1$ and $U/t = 2$, the effective susceptibility $\chi_{\text{cSDW}}^{\text{eff}}$ at $\rho = 0.75$ strongly increases in the low-T region for all system sizes, while $\chi_{\text{cSDW}}^{\text{eff}}$ at $\rho = 0.4$ does not show a similarly strong enhancement and for $U/t = 2$ it
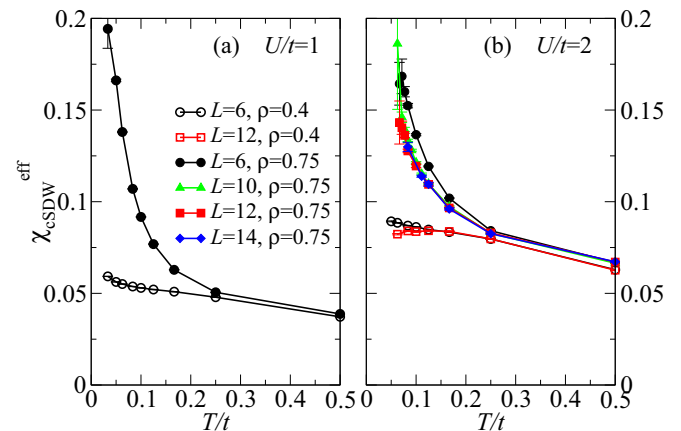

FIG. 11. Temperature dependence of $\chi_{\text{cSDW}}^{\text{eff}}$ at $\rho = 0.4$ and $\rho = 0.75$ for (a) $U/t = 1$ on a $L = 6$ lattice and (b) $U/t = 2$ on $L = 6, 10, 12$, and 14 lattices.
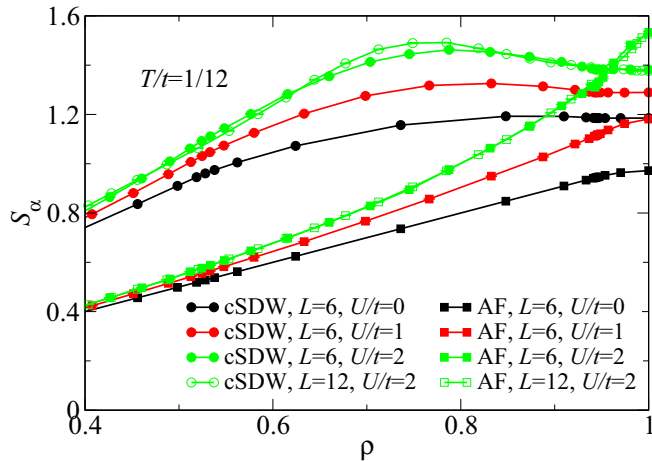
FIG. 12. Structure factors S_{cSDW} and S_{AF} as functions of ρ for several values of U/t for $T/t = 1/12$ on the $L = 6$ lattice. For $U/t = 2$, data for the $L = 12$ lattice are also shown.

FIG. 13. Effective susceptibilities $\chi_{\mathrm{cSDW}}^{\mathrm{eff}}$ and $\chi_{\mathrm{AF}}^{\mathrm{eff}}$ as functions of ρ at $T/t = 1/12$ for (a) $U/t = 1$ on the $L = 6$ lattice and (b) $U/t = 2$ on both $L = 6$ and $L = 12$ lattices.

is even weakly suppressed at low T for the larger system size. Unfortunately, the sign problem does not allow us to perform low-temperature simulations on larger system sizes in order to perform a thorough finite-size scaling analysis of, e.g., S_{cSDW} at low temperatures, which would be required in order to assess if a chiral SDW ground state exists in the thermodynamic limit. Note that this case is different from the case of pairing instabilities, which may, in principle, set in on a *finite* (but still small) low-temperature scale. Nevertheless, our findings provide an indication that at the VHS filling the system may exhibit an instability to the chiral SDW order, whereas away from the VHS filling, this instability is eventually suppressed.

To investigate further how the chiral SDW order behaves at and beyond the VHS filling, we next fix an accessible low temperature $T/t = 1/12$ and monitor how S_{cSDW} and $\chi_{\mathrm{cSDW}}^{\mathrm{eff}}$ vary with the electronic density ρ. For this purpose, Fig. 12 shows S_{cSDW} as a function of ρ for different values of U/t. These results indicate that upon increasing U/t, a peak in S_{cSDW} gradually builds up near the VHS filling, such that the chiral SDW is indeed most pronounced at the VHS filling. This observation agrees with the fact that the three characteristic momentum vectors $\mathbf{Q}_i$, $i = 1,2,3$, of the chiral SDW state form the nesting vectors of the Fermi surface of the noninteracting system at the VHS filling. For comparison, we also show in Fig. 12 the antiferromagnetic structure factor S_{AF}, which, in contrast to S_{cSDW}, displays a monotonic increase with increasing electron density. At half filling, $\rho = 1$, the Hubbard model on the honeycomb lattice is well known to harbor a quantum phase transition to an insulating antiferromagnetic phase for $U/t > 3.76$ [30]. While in Fig. 12, we remain below this critical value of U, the antiferromagnetic correlations already display a clear tendency to grow with increasing U. Furthermore, at $U/t = 2$, the antiferromagnetic structure factor exceeds the chiral SDW structure factor at (and close to) half filling, while upon doping further below half filling, towards the VHS filling, the chiral SDW correlations become more dominant.

We also observe a similar enhancement in the chiral SDW response near the VHS filling for the effective susceptibility
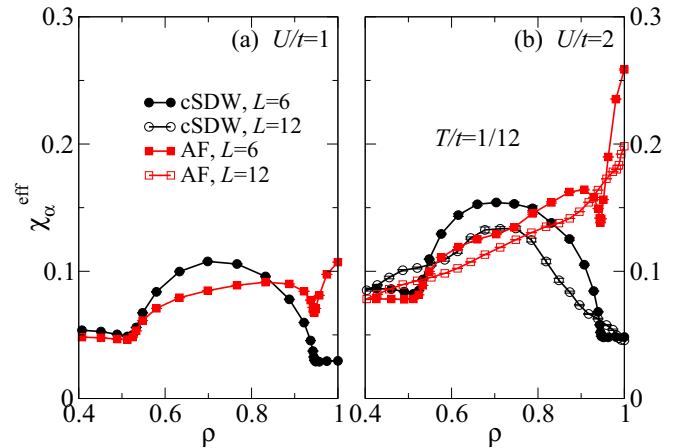
$\chi_{\mathrm{cSDW}}^{\mathrm{eff}}$ (see Fig. 13), strengthening the above interpretation of the structure factor data. Note that in Fig. 13, the $L = 6$ data exhibit two kinks around $\rho \approx 0.5$ and $\rho \approx 0.95$. These appear to be due to finite-size effects (compare to the data for the $L = 12$ lattice, where both kinks are absent). Such peculiar finite-size effects can, in fact, also be observed in a plot of the electronic density as a function of the chemical potential μ in Fig. 14: on the $L = 6$ lattice, the density as a function of μ shows two plateaus near $\rho = 0.5$ and $\rho = 0.95$, whereas on the larger lattice, those plateaus have disappeared. We consider these finite-size plateaus to be the reason for the two kinks seen in Fig. 13 for the $L = 6$ lattice. For the $L = 12$ lattice the density plateaus are absent, and $\chi_{\mathrm{cSDW}}^{\mathrm{eff}}$ decreases steadily upon doping away from the VHS filling, again suggesting that the chiral SDW instability is important when the filling is at (and maybe close to) the VHS value. For comparison, the effective antiferromagnetic susceptibility $\chi_{\mathrm{AF}}^{\mathrm{eff}}$ is also shown in Fig. 13 (where $\chi_{\mathrm{AF}}^{\mathrm{eff}}$ is defined in a way similar to the effective susceptibility for the chiral SDW case). While in the $L = 6$
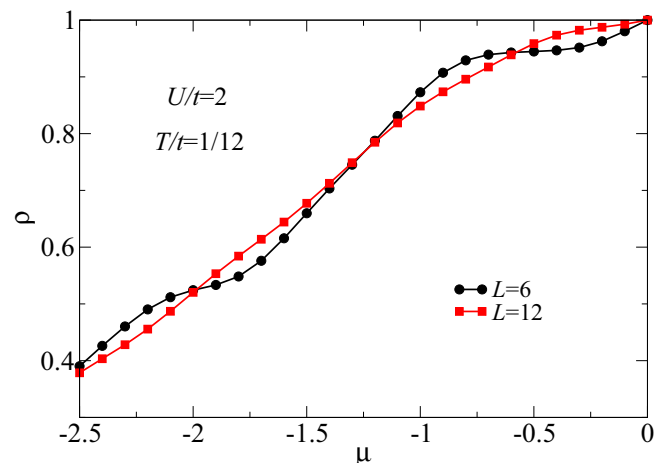

FIG. 14. Electronic density ρ as a function of the chemical potential μ on the $L = 6$ and $L = 12$ lattices for $U/t = 2$ and $T/t = 1/12$.

system this quantity shows finite-size anomalies similar to the effective chiral SDW susceptibility $\chi_{\text{cSDW}}^{\text{eff}}$, in the $L = 12$ system it instead shows a monotonic decease when doping away from half filling, as anticipated from the behavior of the antiferromagnetic structure factor.

V. SUMMARY

To conclude, we used finite-temperature determinantal quantum Monte Carlo simulations to examine the electronic pairing channels and magnetic instabilities of doped graphene within the Hubbard model description. Due to the sign problem, we restricted the study to the weak-coupling regime at the VHS filling, while at lower fillings beyond the VHS, we also accessed the weak- to intermediate-coupling regime. In both cases, we found NN and NNN $(d + id)$-wave pairing to be the dominant pairing channels in the larger system sizes. However, at the VHS filling, we observed strong finite-size effects in the dominant pairing symmetry. This may be taken as an indication that at this filling, due to the logarithmically diverging density of states and a nested Fermi surface, other electronic instabilities may also be relevant. In fact, we observed from measuring appropriate structure factors and magnetic susceptibilities that a previously proposed chiral spin density wave state shows a robust enhancement near the VHS filling but weakens quickly upon doping away from the VHS point. This is in accord with the result in Ref. [31], which suggests on the mean-field level that, upon doping away from a DOS peak, instabilities within the particle-particle channel (superconducting orders) survive decisively longer than those in the particle-hole channel (magnetic or charge orders). We note that a previous study of the Hubbard model on the triangular lattice reported a related result in terms of ferromagnetism and f-wave pairing [32]. For the future, it will be interesting to extend also dynamical cluster approximation studies to consider the competition among the superconducting and magnetic instabilities of the doped honeycomb lattice Hubbard model.

[1] K. S. Novoselov, A. K. Geim, S. V. Morozov, D. Jiang, Y. Zhang, S. V. Dubonos, I. V. Gregorieva, and A. A. Firsov, Science **306**, 666 (2004).

[2] A. H. C. Neto, F. Guinea, N. M. R. Peres, K. S. Novoselov, and A. K. Geim, Rev. Mod. Phys. **81**, 109 (2009).

[3] V. N. Kotov, B. Uchoa, V. M. Pereira, F. Guinea, and A. H. C. Neto, Rev. Mod. Phys. **84**, 1067 (2012).

[4] S. Sorella and E. Tosatti, Europhys. Lett. **19**, 699 (1992).

[5] T. Paiva, R. T. Scalettar, W. Zheng, R. R. P. Singh, and J. Oitmaa, Phys. Rev. B **72**, 085123 (2005).

[6] I. F. Herbut, Phys. Rev. Lett. **97**, 146401 (2006).

[7] I. F. Herbut, V. Juričić, and O. Vafek, Phys. Rev. B **80**, 075432 (2009).

[8] J. L. McChesney, A. Bostwick, T. Ohta, T. Seyller, K. Horn, J. González, and E. Rotenberg, Phys. Rev. Lett. **104**, 136803 (2010).

[9] D. K. Efetov and P. Kim, Phys. Rev. Lett. **105**, 256805 (2010).

[10] For a review see A. M. Black-Schaffer and C. Honerkamp, J. Phys. Condens. Matter **26**, 423201 (2014).

[11] A. M. Black-Schaffer and S. Doniach, Phys. Rev. B **75**, 134512 (2007).

[12] B. Uchoa and A. H. C. Neto, Phys. Rev. Lett. **98**, 146801 (2007).

[13] C. Honerkamp, Phys. Rev. Lett. **100**, 146404 (2008).

[14] S. Pathak, V. B. Shenoy, and G. Baskaran, Phys. Rev. B **81**, 085431 (2010).

[15] T. Watanabe and S. Ishihara, J. Phys. Soc. Jpn. **82**, 034704 (2013).

[16] T. Ma, Z. Huang, F. Hu, and H. Q. Lin, Phys. Rev. B **84**, 121410(R) (2011).

[17] J. P. L. Faye, P. Sahebsara, and D. Senechal, Phys. Rev. B **92**, 085121 (2015).

[18] J. González, Phys. Rev. B **78**, 205431 (2008).

[19] C. A. Lamas, D. C. Cabra, and N. Grandi, Phys. Rev. B **80**, 075108 (2009).

[20] B. Valenzuela and M. A. H. Vozmediano, New J. Phys. **10**, 113009 (2008).

[21] T. Li, Europhys. Lett. **97**, 37001 (2012).

[22] R. Nandkishore, L. S. Levitov, and A. V. Chubukov, Nat. Phys. **8**, 158 (2012).

[23] W. S. Wang, Y. Y. Xiang, Q. H. Wang, F. Wang, F. Yang, and D. H. Lee, Phys. Rev. B **85**, 035414 (2012).

[24] M. L. Kiesel, C. Platt, W. Hanke, D. A. Abanin, and R. Thomale, Phys. Rev. B **86**, 020507(R) (2012).

[25] X. Y. Xu, S. Wessel, and Z. Y. Meng, Phys. Rev. B **94**, 115105 (2016).

[26] R. Blankenbecler, D. J. Scalapino, and R. L. Sugar, Phys. Rev. D **24**, 2278 (1981).

[27] S. R. White, D. J. Scalapino, R. L. Sugar, E. Y. Loh, J. E. Gubernatis, and R. T. Scalettar, Phys. Rev. B **40**, 506 (1989).

[28] V. I. Iglovikov, E. Khatami, and R. T. Scalettar, Phys. Rev. B **92**, 045110 (2015).

[29] S. R. White, D. J. Scalapino, R. L. Sugar, N. E. Bickers, and R. T. Scalettar, Phys. Rev. B **39**, 839 (1989).

[30] S. Sorella, Y. Otsuka, and S. Yunoki, Sci. Rep. **2**, 992 (2012).

[31] T. Löthman and A. M. Black-Schaffer, Phys. Rev. B **96**, 064505 (2017).

[32] S. Q. Su, Z. B. Huang, R. Fan, and H. Q. Lin, Phys. Rev. B **77**, 125114 (2008).